Space–time analysis of actuation transients: Example of plasma-controlled jet flow

Brandon Yeung and Oliver T. Schmidt*
Department of Mechanical and Aerospace Engineering, University of California San Diego, La Jolla, California 92093, USA

(Received 18 September 2025; accepted 19 May 2026; published 22 June 2026)

We outline a workflow for examining statistically transient fluid flows, which eludes most standard modal analysis techniques. As a challenging example, we investigate the forcing-induced transient between statistically stationary and cyclostationary states and discuss the underlying flow physics. The transient dynamics of a turbulent supersonic twin-rectangular jet flow, forced symmetrically at a Strouhal number of 0.9, are studied using synchronized large-eddy simulations. Under plasma-actuated control, the statistically stationary jet evolves towards a cyclostationary state over a transient phase. Forcing-induced perturbations of the natural jet are extracted using synchronized simulations of the natural and forced jets. A database is collected that captures an ensemble of realizations of the perturbations within the initial transient, which is characterized by fast energy growth. The initial pulse of the actuators produces large, impulsive perturbations to the flow field. The mean flow deformation transient reveals that shock cells are deflected by the forcing towards then away from the nozzle, resulting in a subtle but permanent contraction of shock spacings. Despite this, time–frequency analysis shows that jet screech persists throughout the transient. Streamwise wavelet-based filtering of the time-varying mean flow deformation effectively isolates small-scale shock contraction and shear-layer modal instability waves from large-scale but low-amplitude perturbations. The optimal eigenvector from space–time proper orthogonal decomposition is an antisymmetric—or flapping—mode. Applying an analogous filter to the optimal mode, we track the evolution of a large-scale, transient, and dispersive wave-packet structure and observe the coupling of widely disparate scales enabled by spatial inhomogeneity and temporal transience.

DOI: 10.1103/ktxc-hgjf

I. INTRODUCTION

Reducing jet noise is a key challenge in civil and military aviation. Military-style supersonic jets, in particular, can emit intense noise, jeopardizing the health of personnel working in proximity. Although the accurate prediction of jet noise is increasingly attainable [1], controlling jet noise remains more challenging. The focus of this work is the supersonic twin-rectangular jet flow recently investigated by Samimy *et al.* [2]. Their experimental efforts involve the use of localized arc filament plasma actuators (LAFPA) [3] for control and have resulted in good control authority. In parallel, we have recently conducted large-eddy simulations (LES) of the same jet, both unforced and forced [4]. The present study is motivated by applications in jet noise reduction where the sound sources are large-scale coherent structures [5]. We are interested in the controllability of supersonic turbulent jets, in particular, the efficiency with which actuation in the nozzle region can modify noise-emitting

*Contact author: oschmidt@ucsd.edu

vortical perturbations downstream of the nozzle. As a first step towards future control design, in this first of its kind study, we focus on the physics of actuation transients in the plasma-controlled twin jet, with emphasis on the deformation of its mean flow due to forcing.

To date, the vast majority of investigations into turbulent jet forcing for noise reduction have employed either steady or periodic actuation and met with only modest success [6,7]. What is rarely attempted, however, is unsteady and aperiodic actuation. Outside the realm of jet acoustics, such flow control strategies have been rapidly gaining currency, especially in the wake of early demonstrations of genetic programming- [8,9] and (deep) reinforcement learning-based [10–13] control. When the forcing continually adapts to the evolving flow state, the turbulent statistics exhibits transience. Drawing inspiration from these studies, we present a general framework within which flow transience, induced by aperiodic actuation or, as in our case, by the adaptation of an unforced flow to periodic actuation, may be analyzed. Tools designed for high-Reynolds number turbulence typically target long-time statistics; as such, they are not suited to the treatment of the finite-time behavior of actuation transients. We offer a technique tailored to such applications and, for concreteness, demonstrate it on a forced turbulent jet whose statistics evolves from stationarity towards cyclostationarity.

A number of data-driven methods have been proposed to obtain modal decompositions of transient flows. Arguably the most prominent, dynamic mode decomposition (DMD) [14] and its variants have been extensively applied to transient phenomena. Empirical mode decomposition (EMD) [15], designed for transient signals, decomposes data into intrinsic mode functions via the Hilbert–Huang transform. The most common variant of proper orthogonal decomposition (POD) [16], based on the decomposition of spatial correlations only and recently coined as space-only POD [17], has been modified for transient flow analysis [18,19]. For the actuation transient of the high-Reynolds number twin jet, we seek modes that optimally represent spatiotemporal statistics but without imposing an ansatz (purely exponential or oscillatory time dependence, e.g., in the case of DMD [14,20]) on the spatial or temporal evolution of the flow, leaving us with considering a statistical ensemble of transients. Within this ensemble, each realization is effected via the same actuation, which establishes a consistent phase reference. This motivates the use of Lumley's most general form of POD [21,22]. More specifically, we apply space–time POD based on the definition of a finite time horizon [23–26], which is compatible with the original formulation by Lumley. When the more restrictive conditions of statistical stationarity or cyclostationarity are met, the corresponding variant of POD [17,27] should be exploited. Since the actuation transient satisfies neither, only the general space–time form of POD is applicable. A preliminary investigation using this technique steered our main focus towards the time-varying mean of the ensemble as, perhaps surprisingly, variations about the time-varying mean are small.

To better capture the effects of plasma actuation on the unsteady turbulent flow field, we employ the technique of synchronized simulations proposed by Nikitin [28] and independently by Unnikrishnan and Gaitonde [29]. A pair of simulations, with and without actuation, are simultaneously advanced from the same initial condition. In this work, we use synchronized simulations to generate an ensemble of realizations of the deviation of the forced jet from the natural jet, focusing on the initial transient, and then analyze the turbulent statistics of the deviation.

The remainder of this paper is organized as follows. The first part, Sec. II, sets out our methodology, which synthesizes recent advances in space–time statistical techniques. Specifically, Secs. II A and II B recapitulate the methods of synchronized simulations and space–time POD, respectively. These methods are then specialized for studying the flow physics of twin-jet actuation transients in the second part, consisting of Secs. III and IV. The setup of the LES is summarized in Sec. III A. Section III B describes the statistical symmetries of the twin jet. The modeling of plasma actuation is outlined in Sec. III C. The jet dynamics revealed by time-varying mean flow, time–frequency, and space–time POD analyses is reported in Sec. IV and then discussed and summarized in Sec. V.

II. SPATIOTEMPORAL STATISTICS OF FORCED TRANSIENT FLOWS

A. Synchronized simulations

For detailed descriptions of the synchronized simulations technique, we refer the reader to Nikitin [28] and Unnikrishnan and Gaitonde [29]. Here we will only recapitulate the basics. To study the effects of actuation on the statistically stationary but unsteady natural jet, we decompose the solution to the forced compressible Navier–Stokes equations (NSE) as $\boldsymbol{q}_f(\boldsymbol{x},t) = \boldsymbol{q}_n(\boldsymbol{x},t) + \boldsymbol{q}(\boldsymbol{x},t)$, where $\boldsymbol{q}_n(\boldsymbol{x},t)$ is the solution to the natural, unforced NSE and interpreted as an unsteady base state and $\boldsymbol{q}(\boldsymbol{x},t)$ is the perturbation from that base state. Substituting this decomposition into the forced NSE in perturbation form, then removing the unforced NSE, yields the governing equations of the perturbation. In practice, an unforced LES and a forced LES are advanced in parallel from the same initial condition. At each time step, the difference between the two flow states is the solution, $\boldsymbol{q}(\boldsymbol{x},t)$. This by no means amounts to a linearization: We are merely interested in the turbulent statistics of the deviation between the two transients, starting from the same initial condition.

B. Space–time POD

In this section we provide an overview of the space–time POD method, focusing on its application to the analysis of flow transients. We seek the set of modes, $\boldsymbol{\phi}(\boldsymbol{x},t)$, that optimally represent the second-order space–time statistics of the nonergodic, transient process, $\boldsymbol{q}(\boldsymbol{x},t)$, over a finite time window, $t \in [t_0, t_0 + \Delta T]$. Here $\boldsymbol{q}$ represents the perturbation in Sec. II A. In general, $\boldsymbol{q}$ may also be complex. For space–time POD, the process is assumed to have zero expected value, $E\{\boldsymbol{q}(\boldsymbol{x},t)\} = 0$, where $E\{\cdot\}$ denotes the expectation operator. If not, then $E\{\boldsymbol{q}(\boldsymbol{x},t)\}$ must be removed from $\boldsymbol{q}$. As we shall explain in Sec. III C, this expectation accounts for both the statistical ensemble of realizations of $\boldsymbol{q}$ and the inherent spatial symmetry of the statistics.

To obtain the modes, we construct the weighted space–time inner product

$$\langle \boldsymbol{q}_1(\boldsymbol{x},t), \boldsymbol{q}_2(\boldsymbol{x},t)\rangle_{\boldsymbol{x},t} = \int_{t_0}^{t_0+\Delta T}\int_{\Omega} \boldsymbol{q}_2^*(\boldsymbol{x},t)\boldsymbol{W}(\boldsymbol{x},t)\boldsymbol{q}_1(\boldsymbol{x},t)\mathrm{d}\boldsymbol{x}\mathrm{d}t, \tag{1}$$

where Ω is the domain of interest, $(\cdot)^*$ denotes the conjugate transpose, and $\boldsymbol{W}(\boldsymbol{x},t)$ is a Hermitian positive-definite weight tensor. The modes, $\boldsymbol{\phi}(\boldsymbol{x},t)$, maximize the projection

$$\lambda = \frac{E\{|\langle \boldsymbol{q}(\boldsymbol{x},t), \boldsymbol{\phi}(\boldsymbol{x},t)\rangle_{\boldsymbol{x},t}|^2\}}{\langle \boldsymbol{\phi}(\boldsymbol{x},t), \boldsymbol{\phi}(\boldsymbol{x},t)\rangle_{\boldsymbol{x},t}}. \tag{2}$$

As Eq. (2) is the same quantity that is maximized by all variants of space–time POD [21–24], including spectral POD (SPOD) [17,30] and cyclostationary SPOD (CS-SPOD) [27], the solutions, λ_j and $\boldsymbol{\phi}_j$, are given by the standard weighted Fredholm eigenvalue problem,

$$\int_{t_0}^{t_0+\Delta T}\int_{\Omega} \boldsymbol{C}(\boldsymbol{x},\boldsymbol{x}',t,t')\boldsymbol{W}(\boldsymbol{x}',t')\boldsymbol{\phi}(\boldsymbol{x}',t')\mathrm{d}\boldsymbol{x}'\mathrm{d}t' = \lambda\boldsymbol{\phi}(\boldsymbol{x},t), \tag{3}$$

where $\boldsymbol{C}(\boldsymbol{x},\boldsymbol{x}',t,t') = E\{\boldsymbol{q}(\boldsymbol{x},t)\boldsymbol{q}^*(\boldsymbol{x}',t')\}$ is the two-point space–time correlation tensor. Since $\boldsymbol{q}$ is a fluctuation quantity, the eigenvalue, λ_j, measures the fluctuation energy corresponding to the mode, $\boldsymbol{\phi}_j$, under the norm induced by the space–time inner product in Eq. (1). Properties analogous to those of more specialized forms of space–time POD also hold for this most general form; for example, by construction, the modes maintain perfect coherence over space and the finite time window. Unlike SPOD modes, in general, space–time POD modes, $\boldsymbol{\phi}(\boldsymbol{x},t)$, are polychromatic and time-varying. As such, the latter simultaneously provide both a statistical and a dynamical perspective on the evolution of coherent structures.

TABLE I. Parameters of the synchronized simulations: jet Mach number, $M_j = u_j/c_j$, where u_j and c_j are the streamwise velocity and sound speed at the nozzle exit; acoustic Mach number, $M_a = u_j/c_\infty$, where c_∞ is the ambient sound speed; Reynolds number, $\mathrm{Re}_j = \rho_j u_j D_e/\mu_j$, where ρ is the density, μ is the dynamic viscosity, $D_e = 1.6h$ is the equivalent nozzle diameter, and h is the nozzle height; nozzle pressure and temperature ratios, p_t/p_∞ and T_t/T_∞, where $(\cdot)_t$ refers to stagnation quantities; jet temperature ratio, T_t/T_∞; grid size, N_{cv}; and time step, $\mathrm{d}tu_j/h$.

M_j	M_a	Re_j	p_t/p_∞	p_j/p_∞	T_t/T_∞	T_j/T_∞	N_{cv}	$\mathrm{d}tu_j/h$
1.5	1.25	1.07×10^6	3.671	1	1	0.69	76.6×10^6	0.0025

III. TWIN-RECTANGULAR JET FLOW

A. Numerical setup

The parameters of the LES closely follow the setup in our previous study of the forced supersonic twin-rectangular jet [4] and are summarized in Table I. The simulations were carried out using the unstructured compressible solver "Charles" by Cadence [31]. The flow state has been nondimensionalized by the jet exit conditions, denoted $(\cdot)_j$: density by ρ_j, velocities by u_j, temperature by T_j, and pressure by $\rho_j u_j^2$. Lengths are nondimensionalized by the nozzle height, h, and time by h/u_j. Dimensionless frequencies are expressed in terms of Strouhal numbers based on the equivalent nozzle diameter, D_e, i.e., $\mathrm{St} = fD_e/u_j$.

The twin-rectangular nozzle geometry is described thoroughly by Samimy *et al.* [2]. A cavity just upstream of each nozzle lip houses the plasma actuators, with six on each nozzle, consisting of three on the upper lip, and three on the lower lip. The jet flow is nominally ideally expanded but, due to this cavity and the biconical nozzle geometry, contains shocks in the potential core. For more details on the numerical setup, including its validation, we refer the reader to Brès *et al.* [32,33] and Yeung and Schmidt [4].

To obtain multiple independent realizations of the transient, snapshots of the statistically stationary, natural jet are used as initial conditions for the transient simulations. Based on estimates of the two-time autocorrelation, the initial conditions are spaced $(\Delta t)_{\mathrm{IC}} = 100$ apart in time to guarantee their statistical independence. For simplicity and consistency, we set the length of the transient to be the same, $\Delta T = 100$.

Owing to computational limitations, for this study $N = 50$ realizations of the transient were obtained for statistical analysis. Each realization consists of two synchronized simulations: natural and forced. In other words, excluding the collection of initial conditions from one long simulation, a total of 100 simulations were carried out. While a larger statistical ensemble would be desirable, the current sample size is twice that in the space–time POD study of dynamic stall by Kern *et al.* [25]. Snapshots of the five primitive variables, ρ, u, v, w, and T, are extracted from the LES at intervals of $\Delta tu_j/h = 0.25$, then interpolated from the unstructured grid onto a Cartesian grid. The variables are assembled in the state vector $\boldsymbol{q} = [\rho, u, v, w, T]^{\mathrm{T}}$. Since the flow is compressible, we use the weight tensor

$$\boldsymbol{W}(\boldsymbol{x}, t) = \begin{cases} \boldsymbol{W}' & \text{if } t \leqslant 20, \\ 0 & \text{otherwise,} \end{cases} \quad \text{where} \tag{4a}$$

$$\boldsymbol{W}' = \mathrm{diag}\left(\left[\frac{E\{T_n(\boldsymbol{x},t)\}}{\gamma E\{\rho_n(\boldsymbol{x},t)\}M_j^2}, E\{\rho_n(\boldsymbol{x},t)\}, E\{\rho_n(\boldsymbol{x},t)\}, E\{\rho_n(\boldsymbol{x},t)\}, \frac{E\{\rho_n(\boldsymbol{x},t)\}}{\gamma(\gamma-1)E\{T_n(\boldsymbol{x},t)\}M_j^2}\right]\right) \tag{4b}$$

and γ is the adiabatic constant. The inner product in Eq. (1) thus induces the compressible energy norm [34]. Here we use the expectation of the natural jet, since the natural jet is considered the base state in the framework of synchronized simulations. However, in Appendix A we have confirmed that using the expectation of the forced jet instead would have negligible effect on the eigenvalues and eigenvectors. Additionally, we restrict the spatiotemporal norm in Eqs. (1) and (4) to $t \in [0, 20]$

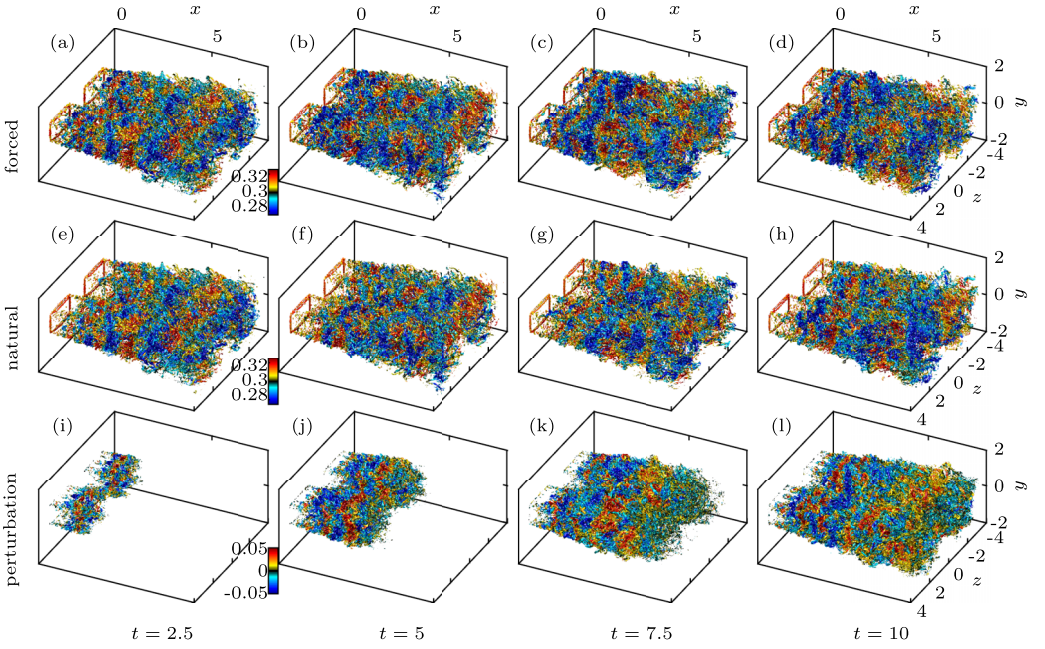

FIG. 1. Q-criterion isocontours of $Q = 5$ at four time instances: [(a), (e), and (i)] $t = 2.5$, [(b), (f), and (j)] $t = 5$, [(c), (g), and (k)] $t = 7.5$, and [(d), (h), and (l)] $t = 10$, computed from velocities [(a)–(d)] $\boldsymbol{u}_f$, [(e)–(h)] $\boldsymbol{u}_n$, and [(i)–(l)] $\boldsymbol{u} = \boldsymbol{u}_f - \boldsymbol{u}_n$. The isocontours are colored by pressure: [(a)–(d)] p_f, [(e)–(h)] p_n, and [(i)–(l)] $p = p_f - p_n$. Panels in each row share the same color bar.

by setting $\boldsymbol{W}(\boldsymbol{x}, t) = 0$ for $t > 20$. The time segment $t \in [0, 20]$ spans approximately 11 actuation periods and focuses on the initial transient. For $t > 20$, the snapshots are included in the dataset but, due to the weighting, do not contribute to the energy as measured by the space–time POD eigenvalues. The outcomes of the space–time POD analysis are inevitably sensitive to the length of this time segment. Indeed, in the long-time limit, we would simply recover the SPOD [17,22,24] or, if the flow is periodically forced, the CS-SPOD [27]. In this limit, contributions to the energy, measured in the spatiotemporal norm, would vanish for the transient phenomena we seek. At the other extreme, in the short-time limit, we would instead recover the space-only POD [17,24]. We must consequently define a time horizon that encapsulates and is tailored to the phenomena of interest. As we shall see in Sec. IV A, the horizon we choose, $t \in [0, 20]$, relates to the length of the potential core.

Instantaneous snapshots of the forced jet, natural jet, and the perturbation are shown in Fig. 1 for one realization of the actuation transient. The snapshots are visualized using the Q criterion [35] and display fully turbulent twin jet plumes. Pressure waves induced by the periodic forcing are visible in the region $x \lesssim 5$ in both the forced jet and the perturbation. Because the perturbation is obtained as the difference between synchronized forced and natural simulations, the evolution of the transient loosely resembles the start-up of a jet exhausting into an initially quiescent medium. For avoidance of doubt, we reiterate that each simulation is initialized from a turbulent, statistically stationary state, not from a laminar base state or a uniform flow.

B. Statistical symmetries

When symmetries are present in a flow, they should be exploited in modal decompositions, including space–time POD. Doing so reduces computational complexity, accelerates statistical convergence, and, perhaps most importantly, improves the interpretability of the results. The twin-

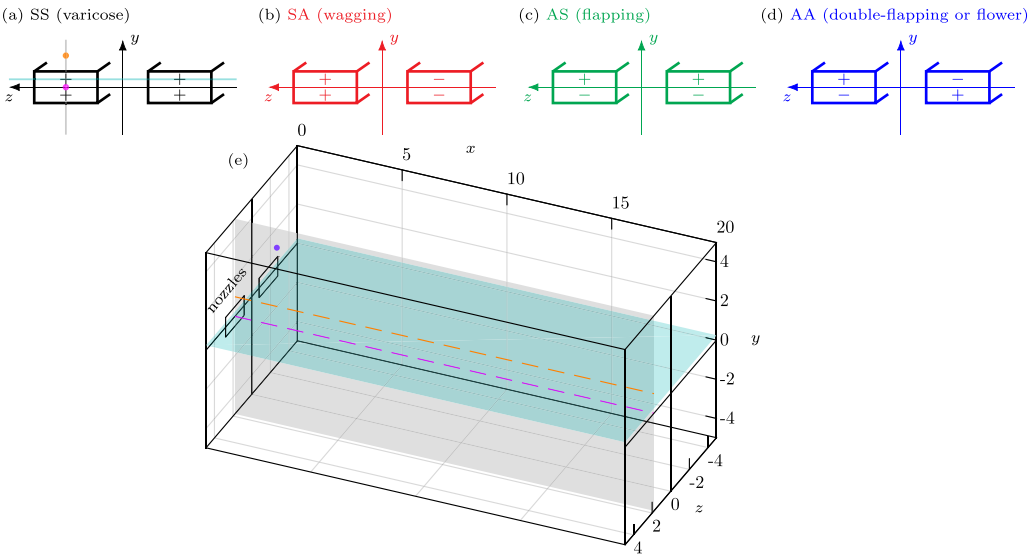

FIG. 2. Illustration of D_2 symmetry decomposition [4] [(a)–(d)] and representative planes, lines, and points (e): [ ] $z = 1.8$; [ ] $y = 0.25$; [ ] nozzle centerline, $(y, z) = (0, 1.8)$; [ ] $(y, z) = (1, 1.8)$; [ ] $(x, y, z) = (2, 4, 1.8)$. Planar projections of these loci are also marked in panel (a).

rectangular jet nozzles are symmetric about the major and minor axes, $y = 0$ and $z = 0$, respectively. The geometry thus belongs in the dihedral group D_2. In the instantaneous flow, geometrical symmetries are broken by turbulence; however, they are imprinted on the turbulent statistics. Nevertheless, when the statistics are estimated from data, these symmetries will be imperfectly expressed and must be enforced. In recent studies, we enforced D_2 symmetry on SPOD of the natural twin-rectangular jet and bispectral mode decomposition [36] of the forced jet [4]. Here we apply the same framework to space–time POD.

Without loss of generality, the perturbations can be decomposed into four D_2 symmetry components (see, e.g., Sirovich and Park [37]),

$$\boldsymbol{q}(x, y, z, t) = \boldsymbol{q}_{\mathrm{SS}}(x, y, z, t) + \boldsymbol{q}_{\mathrm{SA}}(x, y, z, t) + \boldsymbol{q}_{\mathrm{AS}}(x, y, z, t) + \boldsymbol{q}_{\mathrm{AA}}(x, y, z, t), \tag{5}$$

where the first and second letters in the subscripts denote symmetry (S) or antisymmetry (A) about the major and minor axes, respectively. These symmetry components, sometimes referred to as varicose (SS), wagging (SA), flapping (AS), and double-flapping or flower modes (AA) (e.g., Refs. 4,38–42]), are illustrated in Fig. 2(a)–2(d). Following common practice, for each component we conduct an independent analysis using space–time POD. This simplified approach is analogous to the azimuthal Fourier decomposition routinely employed in the analysis of round jets; see, e.g., Arndt *et al.* [43]. It assumes different symmetry components can be examined and interpreted independently.

C. Actuation

The numerical modeling of the plasma actuators, adapted from the actuator model proposed by Kim *et al.* [44], is identical to our recent work on the forced twin jet [4] with the exception of a different actuation frequency. We refer the reader to Yeung and Schmidt [4] for an in-depth

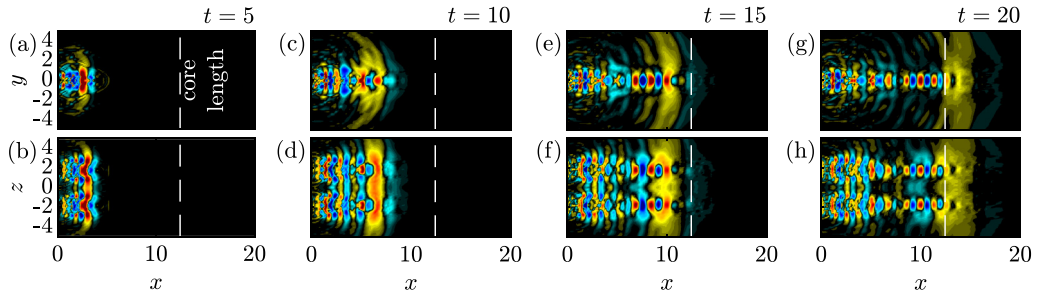

FIG. 3. Pressure component of the mean perturbation: [(a) and (b)] $t = 5$, [(c) and (d)] 10, [(e) and (f)] 15, and [(g) and (h)] 20, visualized on the $z = 1.8$ [(a), (c), (e), and (g)] [in Fig. 2] and $y = 0.25$ [(b), (d), (f), and (h)] [in Fig. 2] planes. The dashed line marks the approximate length of the potential core, $x_{\text{core}} \approx 12.4$. See Supplemental Movie 1 for an animation [46].

exposition and provide only an overview in what follows. The actuation signal,

$$a(t) = \frac{1}{2}\left[\tanh\left(\frac{t - n\tau - t_{\text{on}}}{t_{\text{r}}}\right) - \tanh\left(\frac{t - n\tau - t_{\text{off}}}{t_{\text{r}}}\right)\right], \quad \text{with } n = \left\lfloor \frac{t}{\tau} \right\rfloor, \tag{6}$$

is a smoothed pulse wave with period $\tau = 1.75$. Within each period, the actuator switches on at time $t_{\text{on}} = 0$ and off at time $t_{\text{off}} = 0.001875$, with a rise time of $t_{\text{r}} = 2.5 \times 10^{-5}$. The values for these parameters are estimated based on the available experimental measurements. The duty cycle, $(t_{\text{off}} - t_{\text{on}})/\tau \approx 0.1\%$, is short. As a result, the actuation approximates an impulse train or Dirac comb, which is a periodic but nonharmonic forcing. All harmonics of the actuation frequency, St_0, are thus forced simultaneously. Due to the high forcing amplitude, the forced transient is perturbed substantially with respect to the natural flow. We reemphasize that, departing from the works of Nikitin [28], Unnikrishnan and Gaitonde [29], Adler and Gaitonde [45], and others, we do not attempt to linearize the synchronized system by keeping the perturbation small.

To maximize control authority, the actuation must be consistent with the inherent symmetries of the flow, in this case D_2 symmetry. In the unforced case, the twin-rectangular jet is known to emit screech tones in the AS and AA symmetry components [4]. For this work, we fire all actuators in-phase with each other, corresponding to the SS symmetry. In their experiments, Samimy *et al.* [2] demonstrated reduction in twin-rectangular jet noise using a forcing frequency of $\text{St}_0 = 0.9$. We therefore adopt the same forcing frequency.

Because both the twin-rectangular geometry and the forcing have SS symmetry, the expectation of the flow field, $E\{\boldsymbol{q}(\boldsymbol{x}, t)\}$, is also SS-symmetric. In practice, however, given finite data, the spatial symmetry of $E\{\boldsymbol{q}(\boldsymbol{x}, t)\}$ will be imperfectly captured by the ensemble mean of the realizations of $\boldsymbol{q}$. Upon confirming the approximate SS symmetry of the ensemble mean, we proceed to enforce that symmetry. Specifically, we estimate the expectation by taking the ensemble and spatial mean,

$$E\{\boldsymbol{q}(\boldsymbol{x}, t)\} \approx \widetilde{\boldsymbol{q}_{\text{SS}}(\boldsymbol{x}, t)} = \frac{1}{N}\sum_{k=1}^{N} \boldsymbol{q}_{\text{SS}}^{(k)}(\boldsymbol{x}, t), \tag{7}$$

where $\widetilde{(\cdot)}$ denotes ensemble averaging and the index k denotes the realizations. This quantity is removed from the data prior to space–time POD analysis.

IV. TRANSIENT DYNAMICS AND STATISTICS

A. Mean flow deformation transient

Figure 3 displays the pressure component of the mean of the perturbation, $E\{p(\boldsymbol{x}, t)\}$, at four representative time instances: $t = 5, 10, 15, 20$. At each time instance, the three-dimensional flow

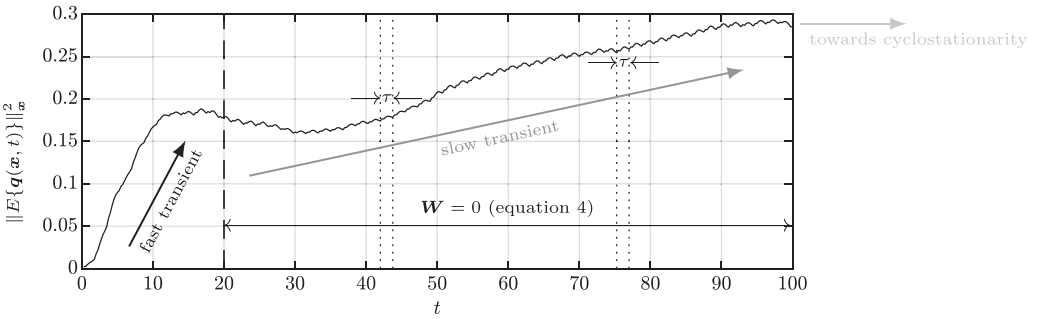

FIG. 4. Spatially integrated energy of the mean perturbation, illustrating three approximate stages of evolution: an initial, fast transient precedes a slow transient, followed by cyclostationarity at large t. The small oscillations correspond to the actuation period, $\tau = 1.75$, as exemplified by the dotted lines. The weight tensor, $\boldsymbol{W}$, ensures data beyond $t = 20$ (dashed line) do not contribute to the space–time POD eigenvalues.

structure is visualized on two different planes: $z = 1.8$, which is parallel to the minor-axis plane, and $y = 0.25$, which is parallel to the major-axis plane. We observe a wave front that is created by the initial pulse of the actuator, corresponding to the response of the natural jet to the impulsive forcing. Subsequent actuation cycles also generate aft-angle acoustic waves at the forcing frequency, St_0, but with significantly lower amplitudes than the impulse response.

In Sec. III A, we alluded to a connection between the finite time horizon of the space–time POD, $t \in [0, 20]$, and the length of the potential core. We now make this connection explicit. Following the procedure outlined by Lakshmi Narasimha Prasad and Unnikrishnan [47], the end of the potential core of the natural jet is estimated as the location along the nozzle centerline where the mean streamwise velocity decays to 90% of its exit-plane value. This location, $x_{\mathrm{core}} \approx 12.4$, is overlaid in Fig. 3. The impulsive wave front propagates through the potential core, surpassing x_{core} approximately at $t = 20$ [Figs. 3(g) and 3(h)]. This provides a natural timescale for the initial transient in which we are interested. We therefore define the horizon as the time for the wave front to traverse the potential core and, as we will shortly discuss, for the shock-cell structure of the natural jet to adjust to the actuation. A complementary view of the initial transient can be gleaned from the energy dynamics of the mean perturbation. Figure 4 traces the time evolution of the energy

$$\|E\{\boldsymbol{q}(\boldsymbol{x},t)\}\|_{\boldsymbol{x}}^2 = \int_\Omega E\{\boldsymbol{q}(\boldsymbol{x},t)\}^* \boldsymbol{W}'(\boldsymbol{x},t) E\{\boldsymbol{q}(\boldsymbol{x},t)\} \mathrm{d}\boldsymbol{x}, \tag{8}$$

measured in the spatial norm $\|\cdot\|_{\boldsymbol{x}}^2$, over the full length of the dataset, $t \in [0, 100]$. The weight $\boldsymbol{W}'$ was defined in Eq. (4b). The energy curve is qualitatively divided into three distinct stages. The initial transient that is the main focus of this study is associated with a short period of fast energy growth. At $t \approx 15$, the initial, fast transient begins transitioning into a longer period of slow dynamics, which persists nearly to the end of the data before plateauing for $t \gtrsim 90$. Superposed on the energy curve for all t are small oscillations at the forcing frequency. In the long-time limit, we therefore expect the statistics to become periodic and the flow to attain cyclostationarity. The horizon $t \in [0, 20]$, during which the impulsive wave front depicted in Fig. 3 traverses the jet core, includes the fast transient and the start of the slow transient.

Behind the impulsive wave front, in the downstream region, $x \gtrsim 5$, of Fig. 3, modes are visible along the centerline of each jet. Close examination of the four time instances reveals that the nodes and antinodes of these modes are largely stationary in space, as we confirm in Fig. 5. These modes are not hydrodynamic in origin. Instead, they result from forcing-induced deformations of the mean flow, specifically the shock-cell structure. Figure 5(a)–5(f) compares the mean of the transients of the natural and forced jets, as well as their difference, along the centerline of one nozzle, at

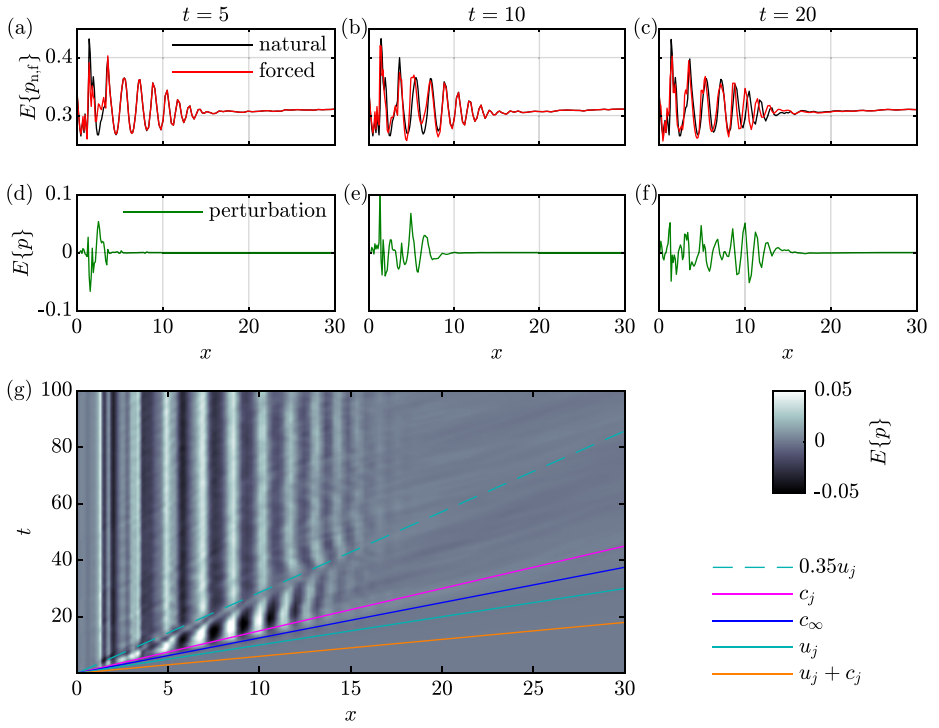

FIG. 5. Mean pressure along the nozzle centerline, $y = 0$ and $z = 1.8$ [– – in Fig. 2]: [(a)–(c)] natural and forced transients; [(d)–(g)] perturbation. Three time instances are displayed: $t = 5$ [(a) and (d)], 10 [(b) and (e)], and 20 [(c) and (f)]. In panel (g), a range of propagation speeds are overlaid for reference. See Supplemental Movie 2 for an animation [46].

$y = 0$ and $z = 1.8$. The streamwise oscillations in Figs. 5(a)–5(c) correspond directly to the shock cells. The deviation between the natural and forced mean flows, quantified in Figs. 5(d)–5(f), propagates downstream from the nozzle. Comparing the two mean flows, we observe that the shock cells in the forced mean (red curves) are shifted upstream from their initial positions in the natural mean (black curves), entailing a slight contraction of the potential core length. Shortening of the potential core in shock-containing jets due to forcing was previously observed by Lakshmi Narasimha Prasad and Unnikrishnan [47]. The phase difference between the shocks of the natural and forced jets explains the wavelike pattern along the centerline of the mean perturbation. To quantify the propagation speed of this deformation, Fig. 5(g) shows the mean perturbation along the centerline as a function of x and t. For visual clarity, the mean perturbation has been smoothed along t using a moving-average filter with a filter width equal to the actuation period, τ. Across most of the x–t plane, the perturbations are approximately vertically oriented, confirming that they are not traveling waves. The most intense perturbations, however, are found near the bottom of the x–t diagram, in a wedge-shaped region in which the stripes are inclined, indicating transient shock deformation. The frontmost (rightmost) boundary of the inclined perturbations lies between the rays corresponding to the jet sound speed, c_j, and the jet velocity, u_j, close to the ambient sound speed, c_∞. This suggests the perturbation front has an acoustic freestream component as well as a component inside the jet, where it interacts with the shear layer and shock cells. The rearmost (leftmost) boundary of the perturbations moves at a velocity of approximately $0.35u_j$. Between the rays $x/t = c_\infty$ and $0.35u_j$ (solid blue and dashed cyan lines, respectively), the shock cells are initially deflected towards the left at $t \approx x/c_\infty$, then shift towards the right, and finally settle into their long-time positions starting at $t \approx x/(0.35u_j)$. For $t \gtrsim x/(0.35u_j)$ (above the dashed

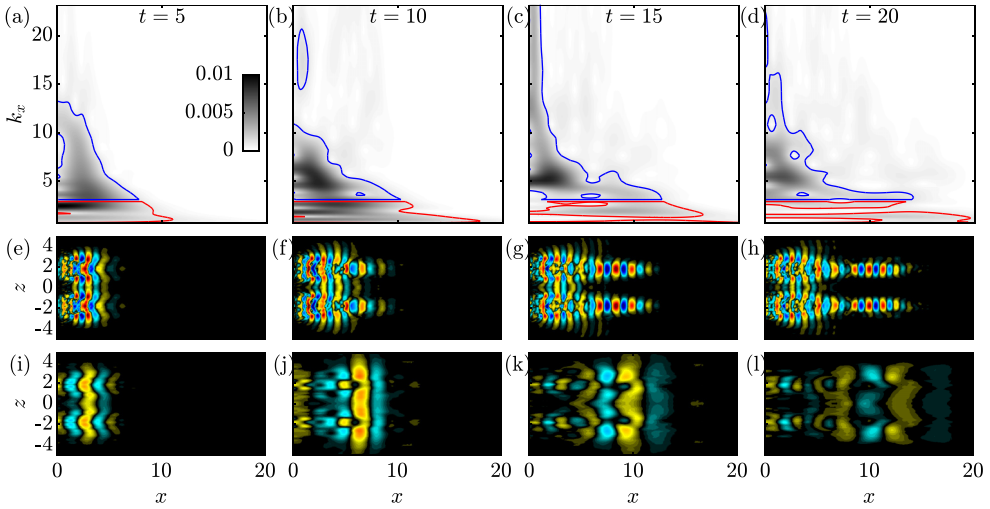

FIG. 6. Streamwise wavenumber decomposition of the mean perturbation in Fig. 3: [(a)–(d)] space–wavenumber scalograms for $(x, y = 1, z = 1.8)$ [in Fig. 2] estimated using the continuous wavelet transform, with high- (blue contour) and low-wavenumber (red contour) thresholds; [(e)–(h)] high-wavenumber component; [(i)–(l)] low-wavenumber component. Each column corresponds to one time instance. The scalograms share the same color bar. The structures are visualized on the $y = 0.25$ plane [in Fig. 2], with a color scale matching Fig. 3.

cyan line), the shocks are stationary and remain slightly—but permanently—deflected from their initial positions in the unforced state. To summarize, the shock-cell structure is initially undisturbed for $t \lesssim x/c_\infty$, undergoes relatively large but transient deformation for $x/c_\infty \lesssim t \lesssim x/(0.35u_j)$, and maintains a smaller but permanent deflection thereafter.

The large-scale wave front and small-scale centerline oscillations in Fig. 3 coexist within the mean perturbation. Nevertheless, the disparity between their spatial scales suggests the two mechanisms may be isolated from each other and visualized separately to aid in their interpretation. Since the mean perturbation is spatially inhomogeneous, we perform a continuous wavelet transform along x for each time instance and each point in the y–z plane. This yields wavelet coefficients localized in x and streamwise wavenumber, k_x. We use the standard Morse family of wavelets. As a representative example, scalograms for the point $y = 1$ and $z = 1.8$ are displayed in Figs. 6(a)–6(d) at four time instances. Coefficients with large magnitudes are mostly localized to small x, but occupy a broad range in k_x. We first filter out the least energetic components of the mean by removing the coefficients with magnitudes below a cutoff of 0.001. Next, we partition the scalograms into high- and low-wavenumber components, respectively small and large scales, using a threshold of $k_x = 3$. The threshold is adjusted by inspection to provide good separation between the two components. Finally, for each component we perform a partial reconstruction from the wavelet coefficients (see, e.g., Farge [48] for details about the inverse wavelet transform). The reconstructions are shown in Figs. 6(e)–6(l). For brevity, only the $y = 0.25$ plane is displayed, as it offers the clearest view of the mean perturbation. The small-scale structure distilled in Figs. 6(e)–6(h) encapsulates two wavelike patterns with comparable wavelengths but distinct spatial support. For $x \lesssim 5.5$, the structure is dominated by Kelvin–Helmholtz-type (KH-type) waves in the shear layer that are phase-locked to the forcing. The relatively high forcing frequency, $\mathrm{St}_0 = 0.9$, explains the short wavelength of the KH-type waves and, by extension, their restriction to the near-nozzle region where the shear layer is thin enough to support them [49,50]. The wavelet-based filtering also clearly reveals aft-angle acoustic radiation coupled to the KH-type waves at all time instances, even near the start of the transient. Along the nozzle centerlines at $z = \pm 1.8$, the shear-layer waves are distorted by the

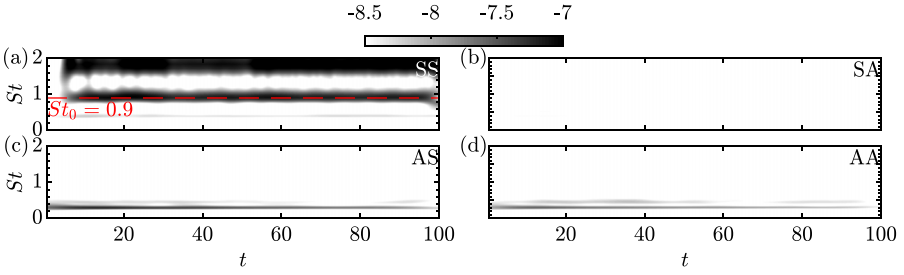

FIG. 7. Ensemble-averaged time–frequency scalograms of the pointwise pressure, $p(x = 2, y = 4, z = 1.8, t)$ [• in Fig. 2], in the forced jet transient for each symmetry component: (a) SS, (b) SA, (c) AS, and (d) AA. The SS forcing frequency, St_0, is marked by the red dashed line.

aforementioned shock-cell shift. Beyond $x \approx 5.5$, the shear-layer waves decay, leaving the shock perturbations as the dominant downstream structure. While the two mechanisms—KH-type waves and shock deformation—are joined in the small-scale structure, they are distinct in origin. The KH-type waves are usually interpreted as a modal instability of the mean flow [51], with the caveat that the mean flow is in this case time-varying. By contrast, the shock perturbations stem from a modification to the mean flow itself.

The reconstructed large-scale structures are shown in Figs. 6(i)–6(l). These waves are lower in amplitude than the small-scale KH-type waves and shock perturbations. In contrast to Fig. 3, the wavelet reconstruction clarifies that the large-scale waves are spatially extended in the streamwise direction. While their amplitude peaks at large x for later time instances, their support extends all the way to the nozzle exit. The waves are also strongly modulated in the transverse direction by the small-scale structures.

The wavenumber decomposition in Fig. 6 confirms that forcing the jet at St_0 elicits a response comprising multiple dominant spatial scales. Those spatial scales are implicitly linked by the dispersion relation of the jet to multiple dominant temporal scales. A multiscale response is consistent with the Dirac comblike actuation signal, which simultaneously excites all harmonics of St_0 (see Sec. III C); it also accords with the impulsive nature [52,53] of the transient forcing, which is capable of inducing a broadband response [54,55].

B. Transient impact on screech acoustics

The impact on acoustics of the actuation transient is symmetry-dependent. Focusing on the forced jet, we next quantify its transient dynamics by conducting a time–frequency analysis. To isolate acoustic disturbances, we extract the pressure signal from a representative probe location in the freestream, $(x, y, z) = (2, 4, 1.8)$, where both the forcing and the screech are well captured. Figure 7 reports the ensemble-averaged continuous wavelet transform of the pressure signal, again using Morse wavelets. In Fig. 7(a), the forced SS component becomes active simultaneously at the fundamental and second harmonic frequencies, St_0 and $2\mathrm{St}_0$, as the acoustic signal from the first actuation cycle reaches the probe after a time delay. The remaining symmetries, however, are not energized at St_0 or its harmonics. The SA symmetry in Fig. 7(b) shows no significant response whatsoever. The AS and AA symmetries in Figs. 7(c) and 7(d) display a screech tone at $\mathrm{St} = 0.3$. This screech is also present in the natural jet. Here we observe a gradual but slight reduction in the screech amplitude over time. We have confirmed that this slow decay also holds true for most of the individual realizations, in addition to their ensemble average. Although screech generation is sensitive to the axial structure of the shock cells [56], the shock deformation observed in Figs. 3 and 5 is very small. The modest impact the actuation has on screech is consistent with the small change in the axial shock spacing.

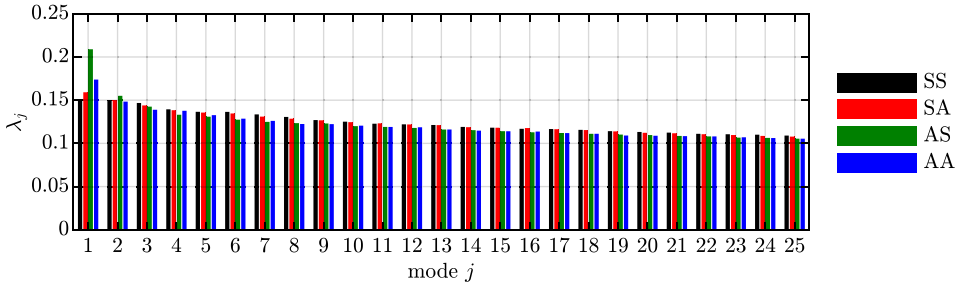

FIG. 8. Space–time POD mode energy for each symmetry component. The horizontal axis is limited to the first 25 modes.

C. Coherent structures in the transient

In Sec. IV A, we examined the spatiotemporal dynamics of the time-varying mean perturbation. We next consider the variance about the mean by performing space–time POD and inspecting a hierarchy of modal energies and structures. The mode energies of each of the four D_2 symmetry components are shown in Fig. 8. Qualitatively, all four symmetries exhibit slow rank decay. The leading mode in the SS, SA, AS, and AA components each accounts for $\lambda_1/\sum_j \lambda_j = 3$–$4\%$ of the total energy in the respective symmetry. This shows that the energetics of the actuation transient are dominated not by the leading mode, but by the mean perturbation, $E\{\boldsymbol{q}(\boldsymbol{x}, t)\}$, with the caveat that dynamically relevant flow structures of low energy may be difficult to converge, especially given the immense computational cost of synchronized LES (see Appendix B). Because the modal energies measure the variance about the mean, the slow decay and low energy indicate that, across different realizations of the transient, the mean perturbation and shock contraction observed in Figs. 3–6 exhibit little variability.

Among the four symmetry components (but excluding the mean perturbation), the AS leading mode contains the most energy, followed by the AA, SA, and SS leading modes. Notably, AS is the only symmetry component possessing a distinct spectral gap between its leading and suboptimal eigenvalues. This phenomenon is consistent with the behavior of the twin-rectangular jet in its statistically stationary, unforced state, in which an AS-symmetric screech mode—a natural flapping instability—is found to dominate [4]. The presence of a (relatively) large spectral gap in the AS component for both the natural and the transiently forced jets hints at a shared mechanism, where a hydrodynamic instability selects for a preferred symmetry.

In the sequel, we focus on the leading AS mode, whose modal structure is reported in Fig. 9. The pressure component is reconstructed using the linearized ideal gas equation of state. Similarly to

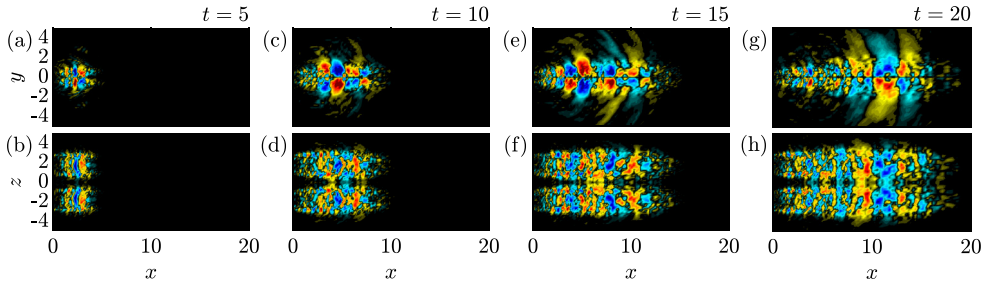

FIG. 9. Pressure component of leading space–time POD mode for AS symmetry: [(a) and (b)] $t = 5$, [(c) and (d)] 10, [(e) and (f)] 15, and [(g) and (h)] 20, visualized on the $z = 1.8$ [(a), (c), (e), and (g)] [in Fig. 2] and $y = 0.25$ [(b), (d), (f), and (h)] [in Fig. 2] planes. See Supplemental Movie 3 for an animation [46].

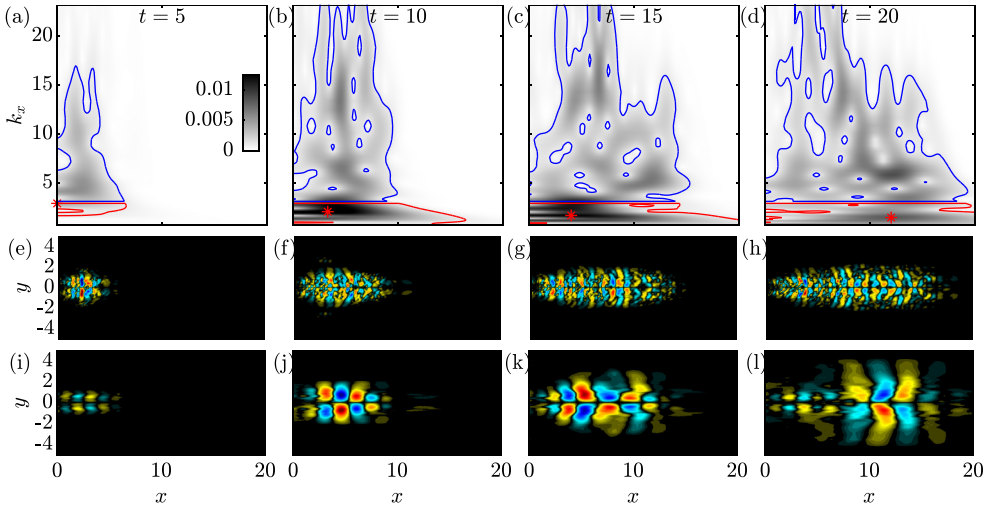

FIG. 10. Same as Fig. 6 but for the leading AS space–time POD mode. In panels (a)–(d), each red asterisk marks the location within the red contour where the scalogram is maximized. The structures are visualized on the $z = 1.8$ plane [in Fig. 2], with a color scale matching Fig. 9.

the behavior of the mean perturbation, the AS mode is dominated by the impulse response from the initial actuation cycle. In contrast to the mean perturbation in Fig. 3, small-scale turbulent structures are generated almost instantaneously in the AS mode in Figs. 9(a) and 9(b). Superimposed on the background turbulence is a dispersive wave packet that emerges in Figs. 9(a) and 9(b) and then increases in wavelength from Figs. 9(a) and 9(b) through Figs. 9(g) and 9(h). Subsequent actuation cycles do not create such a wave packet.

To isolate the transient wave-packet structure from the underlying turbulence, in Fig. 10 we perform wavelet-based high- and low-pass filtering of the leading AS space–time POD mode. The procedure follows what was carried out for the time-varying mean perturbation (see Fig. 6) and, for consistency, the same wavelet coefficient thresholds are used. Compared to the scalograms of the mean perturbation, which peak close to the nozzle and the plasma actuators, the scalograms of the AS mode peak downstream. The scalograms of the mean perturbation exhibit large coefficients for both small and large k_x, reflecting the coexistence of multiple physical mechanisms. By contrast, the AS mode is dominated by small k_x. The reconstructed modal structures are visualized in Figs. 10(e)–10(l) on the $z = 1.8$ plane, where the mode shapes are clearest. We will not interpret the high-wavenumber structure in Figs. 10(e)–10(h), which is of very low amplitude. The low-wavenumber structure in Figs. 10(i)–10(l), on the other hand, effectively distills the wave packet. The peak wavelet coefficient, highlighted by each red asterisk in Figs. 10(a)–10(d), descends in k_x over time. Qualitatively, this suggests the wave packet to be dispersive. The descent in k_x is explained by the spatial development of the shear layer: as the wave packet is advected along x, it experiences a thicker shear layer that supports lower-frequency, larger-scale structures (see, e.g., Schmidt *et al.* [50], Bishop *et al.* [57]). This feature of the wave packet also typifies the capacity of space–time POD modes to represent statistically time-varying coherent structures each containing a range of spatiotemporal scales, in contrast to, e.g., SPOD and DMD modes [14,17,20].

The spatial support of the AS wave packet diverges significantly from that of the SS-symmetric mean perturbation. Figure 11 compares the two in the form of the absolute value of each structure. As noted in Sec. IV A, the mean perturbation displays a double-lobed envelope governed by two distinct mechanisms: KH-type shear-layer waves for small x followed by shock perturbations for large x. Naturally, these mechanisms also have distinct support in the transverse plane. Whereas the near-nozzle shear-layer waves are aligned with the nozzle lips, the downstream shock perturbations

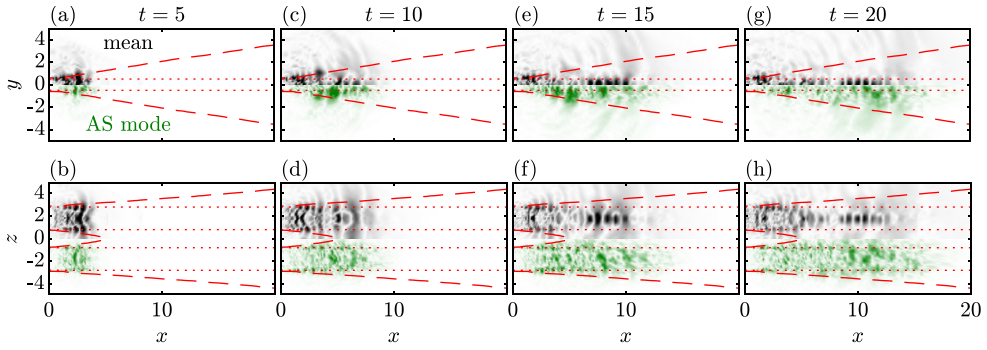

FIG. 11. Absolute value of the pressure component of the mean perturbation (black) and leading AS space–time POD mode (green): [(a) and (b)] $t = 5$, [(c) and (d)] 10, [(e) and (f)] 15, and [(g) and (h)] 20, visualized on the $z = 1.8$ [(a), (c), (e), and (g)] [in Fig. 2] and $y = 0.25$ [(b), (d), (f), and (h)]; [in Fig. 2] planes. Shear-layer widths, estimated from the natural jet as $E\{u_n\} = 0.05$, are marked by red dashes. Lip lines at $y = \pm 0.5$ and $z = \pm 0.8, \pm 2.8$ are marked by red dots.

are confined between the lip lines and lie along the nozzle centerlines. The support of the AS wave packet draws a sharp contrast. Its envelope has a single lobe whose peak streamwise location (also given by the red asterisks in Fig. 10) propagates in the downstream direction. In the transverse plane, the wave packet spans the width of the shear layer and decays gradually in the freestream.

V. DISCUSSION AND SUMMARY

When a statistically stationary turbulent flow is subjected to periodic forcing, it first undergoes a transient state before eventually attaining statistical cyclostationarity. During its transient phase, the statistics of the flow are time-varying and aperiodic. Consequently, to study the actuation transient, we investigate its first- and second-order statistics via the ensemble–spatial mean and the most general form of space–time POD, respectively. We demonstrate this approach on the transients of a plasma-controlled supersonic twin-rectangular jet, periodically and symmetrically forced at $\mathrm{St} = 0.9$. To focus on the perturbations that arise due to the forcing, we conduct synchronized simulations of the natural and forced jets, then measure the statistics of an ensemble of their difference. The difference, or perturbation, visually resembles a jet starting up from an ambient initial condition. Because of this, we expect the present workflow, i.e., examination of the ensemble mean followed by space–time POD (without the need for a baseline), also to be well suited to the analysis of true start-up processes.

The time-varying mean perturbation, which is SS-symmetric, shows that the initial pulse of the actuator has the greatest effect, generating a high-amplitude wave front. The energy contained in the mean perturbation undergoes an initial stage of rapid growth as the jet departs from its unforced, statistically stationary state, followed by slow dynamics that, in the long-time limit, tends towards statistical cyclostationarity. The mean perturbation highlights the mean flow deformation transient occurring near the nozzle centerline; specifically, we identify a brief time window, $x/c_\infty \lesssim t \lesssim x/(0.35u_j)$, during which the shock cells are first deflected towards, then away from, the nozzle. Beyond $t \approx x/(0.35u_j)$, the transient shock movement ceases, and the axial shock spacing remains permanently diminished, albeit only slightly. Time–frequency analysis also reveals a slow decay of the screech amplitude over the length of the data.

In the space–time POD spectra, the AS symmetry is the most energetic and, uniquely, possesses a significant gap between its optimal and suboptimal eigenvalues. In the AS leading mode, the initial actuator pulse gives rise to a large-scale wave packet. The AS mode has an envelope with a single lobe in the streamwise direction; in the transverse plane, the mode has support throughout the shear

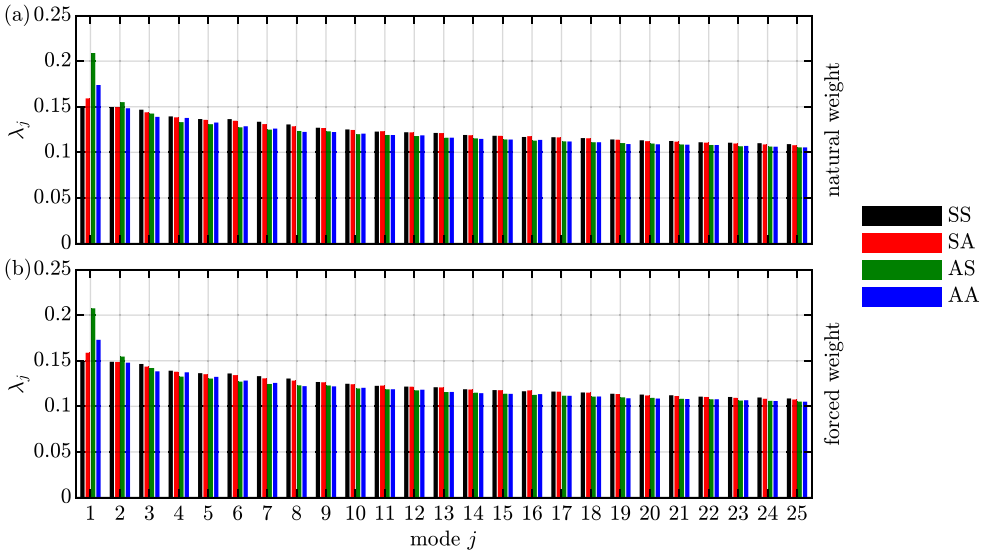

FIG. 12. Space–time POD eigenvalues when the compressible energy weight tensor [34] is obtained via the expectation of (a) the natural jet and (b) the forced jet. Panel (a) repeats Fig. 8 for ease of comparison.

layer. The mean perturbation, by contrast, has two lobes created by waves in the shear layer and shock deformation in the potential core.

As an additional postprocessing step, we subject the mean perturbation and leading AS mode to high- and low-pass filtering in streamwise wavenumber-space, accomplished via a threshold on the wavelet coefficients. The high-wavenumber, small-scale component of the mean perturbation unveils KH-type waves with support in the initial shear layer, followed by shock-cell shifts that dominate downstream in the jet core. The low-wavenumber, large-scale component isolates the transient wave front, clarifies its extended spatial support, and highlights its cross-stream modulation. For the AS mode, the large-scale component isolates the dispersive wave packet, which is characterized by a dominant wavenumber that decreases with time and displacement from the nozzle in accordance with the streamwise development of the shear layer. The mode structure also reveals the coupling of large and small spatiotemporal scales. Such coupling is characteristic of flow inhomogeneities in both space and time, thus requiring a space–time rather than spectral analysis.

The mode in Fig. 9 highlights an obvious limitation when applying space–time POD to transients: a prohibitively large number of realizations may be required to converge the second-order statistics, especially when the data exhibit little low-rankness. Nevertheless, a sample size on the order of 10 is common in similar studies, with computational cost being the main impediment (see, e.g., Kern

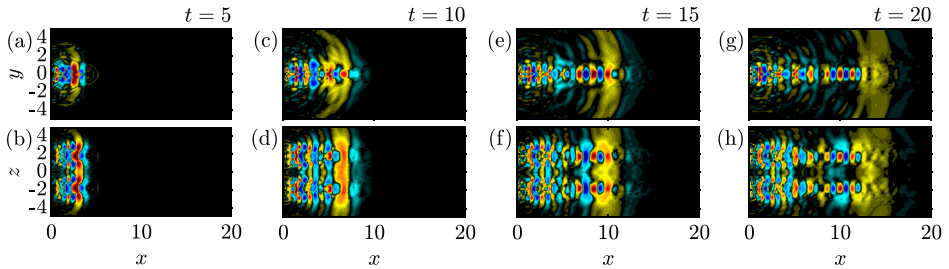

FIG. 13. Same as Fig. 3 but computed from 25 realizations of the transient.

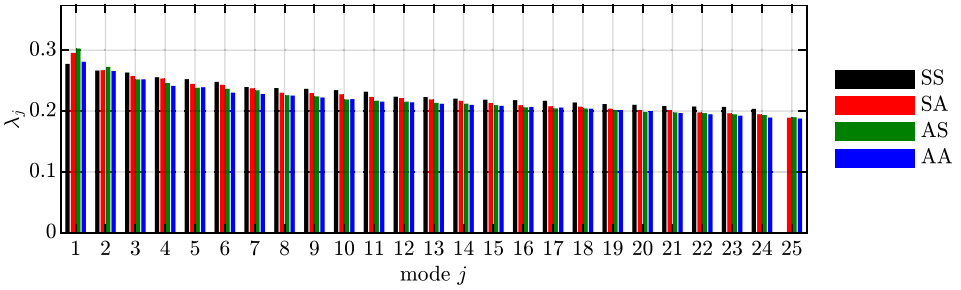

FIG. 14. Same as Fig. 8 but computed from 25 realizations of the transient.

et al. [25]). When an appropriate spatial (circular, reflectional, etc.) symmetry or temporal (periodic, stationary, cyclostationary, etc.) symmetry is known *a priori* and imposed on the decomposition, leveraging the symmetry acts as a powerful filter for the statistics. In the case of a statistically stationary round jet, for instance, the solutions to space–time POD are known to be sinusoidal in both azimuth and time. In this work, with the exception of D_2 symmetry, no solution symmetry is imposed, and the price we pay for generality is slow statistical convergence.

While a dispersive wave packet can be discerned from the AS mode, statistical convergence remains a major caveat to the physical interpretation of the mode (see also Appendix B). In the same vein, all variants of POD inherently focus on the most energetic structures as measured in a specific norm, and not necessarily the physical phenomena of interest that may turn out to possess low energy or be intermittent [14,58]. With these limitations in mind, extending the present analysis to other forcing symmetries and frequencies is currently not tractable, but this remains a subject of interest. Whether general trends exist that lead to statistically transient flows with high variance about the time-varying mean and, perhaps, low-rankness is likewise a topic we plan to assess in future work.

ACKNOWLEDGMENTS

We gratefully acknowledge support from Office of Naval Research Grant No. N00014-23-1-2457, under the supervision of Dr. Steve Martens. LES calculations were carried out on computational resources provided by DoD HPCMP at the ERDC DSRC supercomputer facility. We thank the anonymous referees for their incisive comments.

DATA AVAILABILITY

The data that support the findings of this article are not publicly available upon publication because it is not technically feasible and/or the cost of preparing, depositing, and hosting the data would be prohibitive within the terms of this research project. The data are available from the authors upon reasonable request.

APPENDIX A: WEIGHTING THE SPACE–TIME POD BY THE NATURAL OR FORCED JET

The space–time POD is weighted by the tensor in Eq. (4), which includes the expectations $E\{T(\boldsymbol{x},t)\}$ and $E\{\rho(\boldsymbol{x},t)\}$. In the main text, we choose to evaluate these quantities based on the natural jet. This choice is motivated by the notion in synchronized simulations that the natural flow is the base state to which perturbations are introduced [28,29]. Nonetheless, in this appendix, we demonstrate that weighting the space–time POD by the forced jet in lieu of the natural jet would have negligible impact on the results. Figure 12 compares the two sets of spectra; their distinction is visually imperceptible. The leading modes (not shown) are similarly indistinguishable.

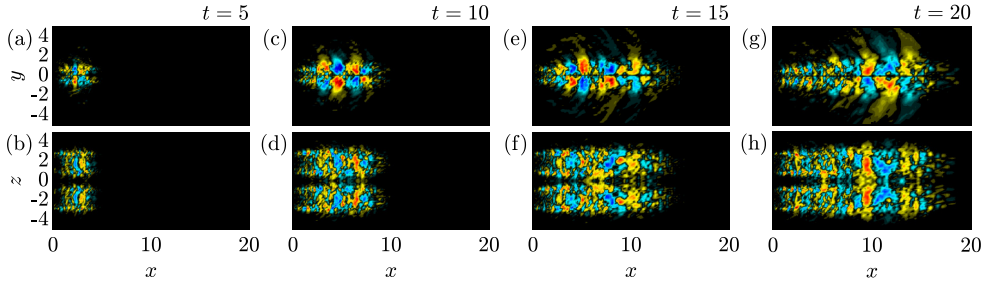

FIG. 15. Same as Fig. 9 but computed from 25 realizations of the transient.

APPENDIX B: STATISTICAL CONVERGENCE

The number of realizations of the transient, 50, used in this study is constrained by computational cost and smaller than is typical for POD analyses. In this appendix, we examine the statistical convergence of the time-varying mean and space–time POD by repeating these computations with the first 25 of 50 realizations. Figure 13 reports the mean perturbation. The contours are marginally less smooth than Fig. 3; otherwise, the two mean flows are in excellent agreement. Figure 14 reports the space–time POD eigenvalues. Compared to Fig. 8, here the eigenvalues have grown in magnitude, because the energy of the perturbation is now partitioned into half as many modes. The qualitative trends discussed in Sec. IV C are preserved: The spectra decay slowly, and the AS leading eigenvalue is the most energetic. We nonetheless observe two discrepancies. First, for AS symmetry, the spectral gap between the first and second eigenvalues, $\lambda_1 - \lambda_2$, is larger in Fig. 8 (50 realizations) than in Fig. 14 (25 realizations). That is, the larger ensemble assists the space–time POD in isolating dominant coherent structures. Second, the leading eigenvalues are ordered as $\lambda_1^{\mathrm{AS}} > \lambda_1^{\mathrm{AA}} > \lambda_1^{\mathrm{SA}} > \lambda_1^{\mathrm{SS}}$ in Fig. 8 but as $\lambda_1^{\mathrm{AS}} > \lambda_1^{\mathrm{SA}} > \lambda_1^{\mathrm{AA}} > \lambda_1^{\mathrm{SS}}$ in Fig. 14. An even greater sample size would thus be needed to disambiguate λ_1^{SA}, λ_1^{AA}, and other lower-energy eigenvalues. Finally, Fig. 15 reports the leading AS mode. While a wave packet similar to that in Fig. 9 can be discerned in Fig. 15, the mode shape here is noticeably less converged. As such, mode convergence with 25 realizations cannot be guaranteed. However, our main physical findings hinge on the well-converged mean.

[1] G. A. Brès and S. K. Lele, Modelling of jet noise: A perspective from large-eddy simulations, Phil. Trans. R. Soc. A **377**, 20190081 (2019).
[2] M. Samimy, N. Webb, A. Esfahani, and R. Leahy, Perturbation-based active flow control in overexpanded to underexpanded supersonic rectangular twin jets, J. Fluid Mech. **959**, A13 (2023).
[3] M. Samimy, I. Adamovich, B. Webb, J. Kastner, J. Hileman, S. Keshav, and P. Palm, Development and characterization of plasma actuators for high-speed jet control, Exp. Fluids **37**, 577 (2004).
[4] B. Yeung and O. T. Schmidt, Spectral dynamics of natural and forced supersonic twin-rectangular jet flow, J. Fluid Mech. **1018**, A34 (2025).
[5] P. Jordan and T. Colonius, Wave packets and turbulent jet noise, Annu. Rev. Fluid Mech. **45**, 173 (2013).
[6] C. A. Brown, Acoustics of excited jets—A historical perspective, J. Acoust. Soc. Am. **118**, 1863 (2005).
[7] B. Henderson, Fifty years of fluidic injection for jet noise reduction, Int. J. Aeroacoust. **9**, 91 (2010).
[8] T. Duriez, V. Parezanovic, J.-C. Laurentie, C. Fourment, J. Delville, J.-P. Bonnet, L. Cordier, B. R. Noack, M. Segond, M. Abel, N. Gautier, J.-L. Aider, C. Raibaudo, C. Cuvier, M. Stanislas, and S. L. Brunton, Closed-loop control of experimental shear flows using machine learning, in *7th AIAA Flow Control Conference* (AIAA, Atlanta, GA, 2014).

[9] T. Duriez, S. L. Brunton, and B. R. Noack, *Machine Learning Control—Taming Nonlinear Dynamics and Turbulence*, Fluid Mechanics and Its Applications Vol. 116 (Springer, Berlin, 2017).
[10] M. Gazzola, B. Hejazialhosseini, and P. Koumoutsakos, Reinforcement learning and wavelet adapted vortex methods for simulations of self-propelled swimmers, SIAM J. Sci. Comput. **36**, B622 (2014).
[11] F. Guéniat, L. Mathelin, and M. Y. Hussaini, A statistical learning strategy for closed-loop control of fluid flows, Theor. Comput. Fluid Dyn. **30**, 497 (2016).
[12] S. Verma, G. Novati, and P. Koumoutsakos, Efficient collective swimming by harnessing vortices through deep reinforcement learning, Proc. Natl. Acad. Sci. USA **115**, 5849 (2018).
[13] J. Rabault, M. Kuchta, A. Jensen, U. Réglade, and N. Cerardi, Artificial neural networks trained through deep reinforcement learning discover control strategies for active flow control, J. Fluid Mech. **865**, 281 (2019).
[14] P. J. Schmid, Dynamic mode decomposition of numerical and experimental data, J. Fluid Mech. **656**, 5 (2010).
[15] N. E. Huang, Z. Shen, S. R. Long, M. C. Wu, H. H. Shih, Q. Zheng, N.-C. Yen, C. C. Tung, and H. H. Liu, The empirical mode decomposition and the Hilbert spectrum for nonlinear and non-stationary time series analysis, Proc. R. Soc. Lond. A **454**, 903 (1998).
[16] L. Sirovich, Turbulence and the dynamics of coherent structures part I: Coherent structures, Quart. Appl. Math. **45**, 561 (1987).
[17] A. Towne, O. T. Schmidt, and T. Colonius, Spectral proper orthogonal decomposition and its relationship to dynamic mode decomposition and resolvent analysis, J. Fluid Mech. **847**, 821 (2018).
[18] B. R. Noack, K. Afanasiev, M. Morzyński, G. Tadmor, and F. Thiele, A hierarchy of low-dimensional models for the transient and post-transient cylinder wake, J. Fluid Mech. **497**, 335 (2003).
[19] M. A. Mendez, M. Balabane, and J.-M. Buchlin, Multi-scale proper orthogonal decomposition of complex fluid flows, J. Fluid Mech. **870**, 988 (2019).
[20] C. W. Rowley, I. Mezić, S. Bagheri, P. Schlatter, and D. S. Henningson, Spectral analysis of nonlinear flows, J. Fluid Mech. **641**, 115 (2009).
[21] J. L. Lumley, The structure of inhomogeneous turbulent flows, in *Atmospheric Turbulence and Radio Propagation*, edited by A. M. Yaglom and V. I. Tatarski (Nauka, Moscow, 1967), pp. 166–178.
[22] J. L. Lumley, *Stochastic Tools in Turbulence* (Academic Press, New York, 1970).
[23] O. T. Schmidt and P. J. Schmid, A conditional space–time POD formalism for intermittent and rare events: example of acoustic bursts in turbulent jets, J. Fluid Mech. **867**, R2 (2019).
[24] P. Frame and A. Towne, Space–time POD and the Hankel matrix, PLoS One **18**, e0289637 (2023).
[25] J. S. Kern, D. C. P. Blanco, A. V. G. Cavalieri, P. S. Negi, A. Hanifi, and D. S. Henningson, Direct numerical simulations of an airfoil undergoing dynamic stall at different background disturbance levels, J. Fluid Mech. **986**, A3 (2024).
[26] O. T. Schmidt, Data-driven forecasting of high-dimensional transient and stationary processes via space–time projection, Proc. R. Soc. A **482**, 20250454 (2026).
[27] L. Heidt and T. Colonius, Spectral proper orthogonal decomposition of harmonically forced turbulent flows, J. Fluid Mech. **985**, A42 (2024).
[28] N. Nikitin, On the rate of spatial predictability in near-wall turbulence, J. Fluid Mech. **614**, 495 (2008).
[29] S. Unnikrishnan and D. V. Gaitonde, A high-fidelity method to analyze perturbation evolution in turbulent flows, J. Comput. Phys. **310**, 45 (2016).
[30] O. T. Schmidt and T. Colonius, Guide to spectral proper orthogonal decomposition, AIAA J. **58**, 1023 (2020).
[31] G. A. Brès, F. E. Ham, J. W. Nichols, and S. K. Lele, Unstructured large-eddy simulations of supersonic jets, AIAA J. **55**, 1164 (2017).
[32] G. A. Brès, B. C. Y. Yeung, O. T. Schmidt, A. Esfahani, N. Webb, M. Samimy, and T. Colonius, Towards large-eddy simulations of supersonic jets from twin rectangular nozzle with plasma actuation, in AIAA AVIATION 2021 Forum (AIAA, Virtual, 2021).

[33] G. A. Brès, S. T. Bose, C. B. Ivey, M. Emory, and F. Ham, GPU-accelerated large-eddy simulations of supersonic jets from twin rectangular nozzle, in *28th AIAA/CEAS Aeroacoustics 2022 Conference* (AIAA, Southampton, UK, 2022).
[34] B.-T. Chu, On the energy transfer to small disturbances in fluid flow (part I), Acta Mech. **1**, 215 (1965).
[35] J. C. R. Hunt, A. A. Wray, and P. Moin, Eddies, streams, and convergence zones in turbulent flows, in *Proceedings of the Summer Program 1988* (Center for Turbulence Research, Stanford, CA, 1988), pp. 193–208.
[36] O. T. Schmidt, Bispectral mode decomposition of nonlinear flows, Nonlin. Dyn. **102**, 2479 (2020).
[37] L. Sirovich and H. Park, Turbulent thermal convection in a finite domain: Part I. Theory, Phys. Fluids **2**, 1649 (1990).
[38] P. J. Morris, Instability of elliptic jets, AIAA J. **26**, 172 (1988).
[39] K. W. Kinzie and D. K. McLaughlin, Azimuthal mode measurements of elliptic jets, Phys. Fluids **9**, 2000 (1997).
[40] P. Nogueira, J. Beekman, J. Weightman, and D. Edgington-Mitchell, On the waves underpinning screech in rectangular jets, in *AIAA AVIATION 2023 Forum* (AIAA, San Diego, CA, 2023).
[41] F. R. Amaral, P. Jordan, M. Avanci, J.-C. Robinet, J. Huber, and G. Pont, Coherent structures in subsonic elliptical jets, in *30th AIAA/CEAS Aeroacoustics Conference* (AIAA, Rome, Italy, 2024).
[42] G. Lu, J. Beekman, S. Mazharmanesh, D. Edgington-Mitchell, and P. Nogueira, Modelling rectangular-jet screech via dimensional reduction, Theor. Comput. Fluid Dyn. **40**, 1 (2026).
[43] R. E. A. Arndt, D. F. Long, and M. N. Glauser, The proper orthogonal decomposition of pressure fluctuations surrounding a turbulent jet, J. Fluid Mech. **340**, 1 (1997).
[44] J. Kim, A. Afshari, D. J. Bodony, and J. B. Freund, LES investigation of a Mach 1.3 jet with and without plasma actuators, in *47th AIAA Aerospace Sciences Meeting including The New Horizons Forum and Aerospace Exposition* (AIAA, Orlando, FL, 2009).
[45] M. C. Adler and D. V. Gaitonde, Dynamic linear response of a shock/turbulent-boundary-layer interaction using constrained perturbations, J. Fluid Mech. **840**, 291 (2018).
[46] See Supplemental Material at http://link.aps.org/supplemental/10.1103/ktxc-hgjf for movies.
[47] A. Lakshmi Narasimha Prasad and S. Unnikrishnan, Active control of an overexpanded jet using plasma-based actuators, Phys. Rev. Fluids **10**, 024602 (2025).
[48] M. Farge, Wavelet transforms and their applications to turbulence, Annu. Rev. Fluid Mech. **24**, 395 (1992).
[49] D. Jung, S. Gamard, and W. K. George, Downstream evolution of the most energetic modes in a turbulent axisymmetric jet at high Reynolds number. Part 1. The near-field region, J. Fluid Mech. **514**, 173 (2004).
[50] O. T. Schmidt, A. Towne, G. Rigas, T. Colonius, and G. A. Brès, Spectral analysis of jet turbulence, J. Fluid Mech. **855**, 953 (2018).
[51] D. G. Crighton and M. Gaster, Stability of slowly diverging jet flow, J. Fluid Mech. **77**, 397 (1976).
[52] P. Huerre and P. A. Monkewitz, Local and global instabilities in spatially developing flows, Annu. Rev. Fluid Mech. **22**, 473 (1990).
[53] P. J. Schmid, Nonmodal stability theory, Annu. Rev. Fluid Mech. **39**, 129 (2007).
[54] I. Delbende, J.-M. Chomaz, and P. Huerre, Absolute/convective instabilities in the Batchelor vortex: A numerical study of the linear impulse response, J. Fluid Mech. **355**, 229 (1998).
[55] M. Jovanović and B. Bamieh, The spatio-temporal impulse response of the linearized Navier–Stokes equations, in *Proceedings of the 2001 American Control Conference* (IEEE, Arlington, VA, 2001), Vol. 3, pp. 1948–1953.
[56] D. Edgington-Mitchell, X. Li, N. Liu, F. He, T. Y. Wong, J. Mackenzie, and P. Nogueira, A unifying theory of jet screech, J. Fluid Mech. **945**, A8 (2022).
[57] K. A. Bishop, J. E. Ffowcs Williams, and W. Smith, On the noise sources of the unsuppressed high-speed jet, J. Fluid Mech. **50**, 21 (1971).
[58] C. W. Rowley, Model reduction for fluids, using balanced proper orthogonal decomposition, Int. J. Bifurcat. Chaos **15**, 997 (2005).